Electrical and microstructural properties of Yb-doped CeO$_2$

B. Matović [a], M. Stojmenović [a], J. Pantić [a], A. Varela [b], M. Žunić [b], N. Jiraborvornpongsa [c], T. Yano [c,*]

[a] Institute of Nuclear Sciences "Vinča", Materials Science Laboratory, University Belgrade, Serbia
[b] Instituto de Química, Universidade Estadual Paulista Júlio de Mesquita Filho, Rua Prof. Francisco Degni, 55, CEP 14800-900 Araraquara, Sao Paolo, Brazil
[c] Tokyo Institute of Technology, Research Laboratory for Nuclear Reactors, 2-12-1, Ookayama, Meguro-ku, Tokyo, Japan

ABSTRACT

Nanopowdered Ce$_{1-x}$Yb$_x$O$_{2-\delta}$ solid solutions ($0 \le x \le 0.2$) were synthesized by a self-propagating room temperature synthesis. XRD and SEM were used to study the properties of these materials as well as the Yb solubility in CeO$_2$ lattice. Results showed that all the obtained powders were solid solutions with a fluorite-type crystal structure and with nanometric particle size. The average size of Ce$_{1-x}$Yb$_x$O$_{2-\delta}$ particles was approximately 3 nm. Electrochemical impedance spectroscopy for the sintered pellets depicted that it was possible to separate R_{bulk} and R_{gb} in the temperature interval of 550–800 °C. The activation energy for the bulk conduction was 1.03 eV and for grain boundary conduction was 1.14 eV. Grain boundary resistivity dominates over the other resistivities. These measurements confirmed that Yb^{3+}-doped CeO$_2$ material had a potential as electrolyte for intermediate-temperature solid oxide fuel cell applications.

© 2014 The Ceramic Society of Japan and the Korean Ceramic Society. Production and hosting by Elsevier B.V. All rights reserved.

1. Introduction

Cerium oxide (CeO$_2$) has been widely investigated because of its various applications such as a catalyst, an insulating layer on silicon substrate, a material of high refractive index, an ultraviolet absorber, a hydrogen storage material, an oxygen sensor, a mechanical polishing medium, and an additive to other high-tech ceramics [1–8]. One of the most promising applications of CeO$_2$ based ceramics is the fabrication of electrolyte material for solid oxide fuel cell (SOFC). Several ionically conducting ceramics are currently employed as SOFC materials. The most effective of these are based on aliovalently substituted zirconia and ceria. It is important to note that for comparable doping conditions, the overall oxygen ionic conductivity in doped ceria is approximately an order of magnitude greater than that of stabilized zirconia [9].

The larger ionic radius of Ce^{4+} (97 pm) than Zr^{4+} (72 pm) [10] results in much more open structure through which oxygen ions can easily migrate [11]. This allows CeO$_2$ to be used as an electrolyte at moderate operating temperatures. Another advantage of ceria-based systems is ceria's activity which is a result of its ability to partially change oxidation state from Ce^{4+} to Ce^{3+} during the reaction from Ce^{4+}O$_2$ to Ce$_{1-x}$$^{4+}Ce_x$$^{3+}O_{2-x/2}$. This process can be modified by partial substitution of Ce^{4+} with trivalent rare-earth ions. The ionic conductivity of an electrolyte strongly depends on properties of dopant, namely, concentration, ionic radius and formal charge [12]. Partial replacement of Ce^{4+} ions with di- or triovalent ions produces a large density of oxygen vacancies in ceria lattice enhancing the ionic conductivity of these materials [13,14]. The ionic conductivity of CeO$_2$ ceramics doped with various ions (Ca^{2+}, Sr^{2+}, Ba^{2+}, Y^{3+}, Ln^{3+}, Sm^{3+}, Gd^{3+}, Nd^{3+}) at different concentrations has been extensively investigated. Moreover, there is a concept of the matching radius, which is developed based on minimal difference between the host Ce^{4+} and dopant cation [15]. The concept suggests that ionic conductivity could be enhanced by a decrease of ionic radius mismatch [15]. Therefore, the high quality electrolyte should be non-distorted fluorite crystal lattice. Bearing this in mind it is expected that the best candidate would be trivalent ions with approximately the same radius as the cerium ion. The radius of ytterbium ion is the closest to the radius of cerium ion. According to Shannon's compilation [10], the ionic radii of Ce^{4+} and Yb^{3+} for coordination number (CN) 8 are 97 and 98.5 pm, respectively. Therefore, the main idea of this work is that doping ceria with slightly larger sized Yb^{3+} ion will keep almost the same lattice constant as an undoped ceria and will increase ionic conductivity of ceria as a consequence of oxidation state difference between Ce^{4+} and Yb^{3+}.

The other important parameter in design of modified ceria ceramics is the preparation method of powders. Among many methods that have been employed to produce doped cerium

* Corresponding author. Tel.: +81 3 5734 3380; fax: +81 3 5734 2959.
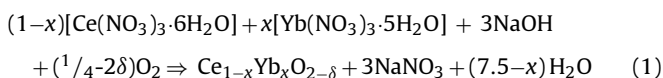E-mail address: tyano@nr.titech.ac.jp (T. Yano).
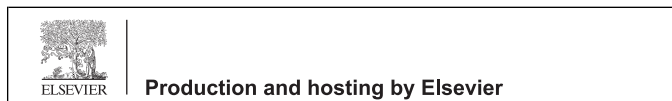
oxide nanoparticles [16–21], one of the methods that is cost and time effective is the self-propagating room temperature (SPRT) synthesis of powders [22–24]. SPRT procedure is based on the self-propagating room temperature reaction between metal nitrates and sodium hydroxide.

Since there is a lack of literature data about ytterbium as a dopant ion in ceria solid solution, in the present study, we report SPRT method for preparation of nano-crystalline powders of Yb-doped ceria. Also in order to develop a new electrolyte for intermediate temperature SOFC, the ionic conductivity of some compositions of Yb-doped ceria was studied.

2. Experimental procedures

Nanopowders $Ce_{1-x}Yb_xO_{2-\delta}$ ($0 \leq x \leq 0.2$) were synthesized by a self-propagating room temperature synthesis [22–24]. Starting reactants were $Ce(NO_3)_3 \cdot 6H_2O$ (Aldrich, 99.999%), $Yb(NO_3)_3 \cdot 5H_2O$ (Aldrich, 99.999%) and NaOH. The compositions of the starting reacting mixtures were calculated according to the nominal composition of the final reaction product. Synthesis is done according to the following overall reaction:

$$(1-x)[Ce(NO_3)_3 \cdot 6H_2O] + x[Yb(NO_3)_3 \cdot 5H_2O] + 3NaOH$$

$$+ (^1/_4 - 2\delta)O_2 \Rightarrow Ce_{1-x}Yb_xO_{2-\delta} + 3NaNO_3 + (7.5-x)H_2O \qquad (1)$$

The X-ray powder analysis is used to identify the crystalline phases as well as lattice parameters of solid solutions of obtained powders. Powder XRD patterns of samples heat treated at different temperatures were recorded on Siemens D-500 X-ray diffractometer with Ni-filtered Cu $K\alpha_{1,2}$ radiation. The measurements were performed in the 2θ range from $20°$ to $80°$ in a continuous scan mode with a step width of $0.02°$ and at a scan rate of $2°$/min. Calculation of the average crystallite size (D) was performed on the basis of the full-width at half-maximum intensity (FWHM) of the 1 1 1, 2 0 0, 2 2 0 and 3 1 1 reflections of CeO_2 by using Scherrer's formula [25]:

$$D_{hkl} = \frac{K\lambda}{\beta \cos\theta} \qquad (2)$$

where λ is the wavelength of the X-rays, K is a constant approximately equal to 1 and set as 0.9 in this study, θ is diffraction angle, $\beta = (\beta_m - \beta_s)$, β is corrected half-width for instrumental broadening, β_m observed half-width and β_s is half-width of the standard CeO_2 sample. Values of lattice parameters of all powders were calculated from the position of the observed diffraction lines based on collected XRD data according to the formula:

$$\frac{4\sin^2\theta}{\lambda^2} = \frac{1}{d_{hkl}^2} = \frac{h^2 + k^2 + l^2}{a^2} \qquad (3)$$

In this equation, a indicates the lattice parameter of the cubic crystal lattice and h, k and l are the Miller indices of the considered Bragg reflection.

Scanning electron microscopy (FE-SEM, field-emission type, S-4800, Hitachi, Japan or JSM 6330F, JEOL, Japan) was used for morphology image of powders or sintered samples.

Powders were isostatically pressed at 70 MPa and sintered in air at 1500 °C for 1 h, with a heating rate of 4 °C/min. Thermogravimetric and thermodifferential analyses (DTA/TGA) were performed using a Mettler Toledo TGA/SDTA851 equipment at a heating rate of 10 °C/min in air with typically 20 mg sample.

After sintering of sample, the platinum paste was painted on the both sides of sintered sample and electrochemical impedance spectroscopy (EIS) measurements were carried out in the 550–800 °C temperature range using a frequency response analyzer (FRA

Solartron 1260), coupled with a dielectric interface (Solartron 1296), in a frequency range between 0.1 Hz and 5 MHz with an AC voltage amplitude of 50 mV. The impedance plots were fitted by ZView® for Windows software (Version 3.2b).

3. Results and discussion

Typical XRD patterns for the Yb-doped CeO_2 with different dopant concentrations are shown in Fig. 1. Peaks related to isolated Yb-phases were not observed and all XRD patterns could be indexed satisfactory to the fluorite crystal structure with space group $Fm3m$. XRD analysis revealed that all peaks for each sample were significantly broadened, indicating small crystallite size and/or strain. It exhibited very diffuse diffraction lines, in such way that some atomic planes were impossible to indicate ($h k l$: 2 2 2, 4 0 0, 3 3 1, 4 2 0). The values of the lattice parameters and crystallite size for all the samples are listed in Table 1. It could be seen that lattice parameter increased with an increase in the dopant concentration. As we mentioned before, according to Shannon's compilation [10], the ionic radii of Ce^{4+} and Yb^{3+} for CN = 8 are 97 and 98.5 pm, respectively. Thus, doping with a slightly larger sized Yb^{3+} ions will increase the lattice parameter of ceria and with increasing of Yb ion concentration the cubic ceria lattice will expand. On the other hand, Yb and induced corresponding oxygen vacancies generate the internal stress in the ceria matrix. Measurement of the full-width at half-maximum (FWHM) for the 1 1 1 reflection confirmed this assumption, showing that increasing the dopant concentration increased FWHM value (Table 1). Crystallite size, calculated on the basis of XRD data, for all powders lays below 3 nm (Table 1).

Literature data show that an increase in concentration of Yb leads to an increase in ionic conductivity [26], achieving the highest value in composition with 20% Yb [26,27]. Since the application of solid solutions of ceria for solid electrolyte showed the best properties for doping concentration of 20%, all the other studies were done with ceria doped with 20% Yb.
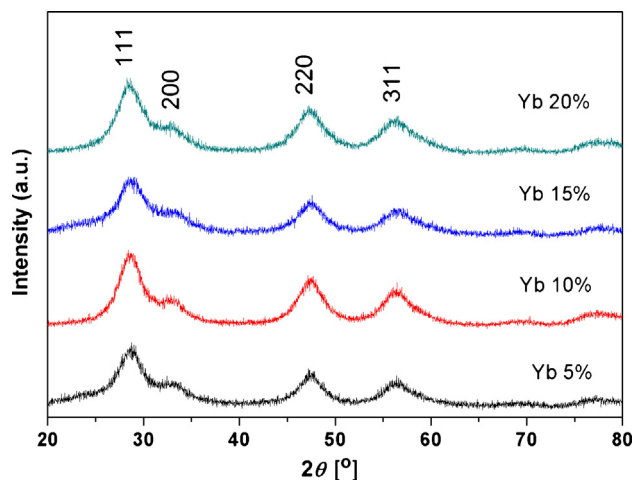

Fig. 1. XRD patterns of the as prepared $Ce_{1-x}Yb_xO_{2-\delta}$ nanopowders with various Yb concentrations.

Table 1
Crystallite size (D), lattice parameters (a) and full width at half-maximum (FWHM) of $Ce_{1-x}Yb_xO_{2-\delta}$ nanopowders with various Yb concentrations.

Yb concentrations (%)	FWHM	a (nm)	D (nm)
5	3.013	0.5429	2.8
10	3.088	0.5432	2.7
15	3.234	0.5434	2.6
20	3.487	0.5466	2.4

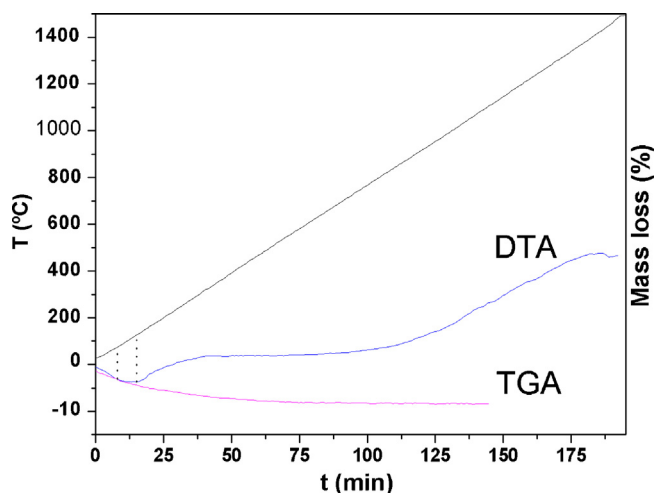**Fig. 2.** DTA and TGA curves of $Ce_{0.80}Yb_{0.20}O_{2-\delta}$ powder obtained by SPRT method at heating rate of 10 °C/min in air.

Fig. 3. XRD patterns of the $Ce_{0.80}Yb_{0.20}O_{2-\delta}$ powders calcined at different temperatures.

DTA analysis of obtained ceria powder doped with 20% Yb showed very broad exothermic peak in the range of 80–130 °C, followed by weight loss of ~4 wt.% (Fig. 2). This behavior corresponded to the evaporation of absorbed water from ceria nanopowder. Further increase in temperature showed no change in the mass, indicating high stability of the ceria solid solution.

In order to study the effect of annealing temperature on crystallite size, the as-prepared powder was annealed at 300, 600 and 900 °C for 4 h in air (Fig. 3). The annealed powders depicted sharpening of diffraction lines due to the increase in crystallite size. The value of FWHM decreased from 1.82 for powder annealed at 300 °C to 0.21 for powder annealed at 900 °C. Although the powder annealed at 900 °C was well crystallized (Fig. 3), there was no appearance of any secondary phase. The results of change of crystallite size with annealing temperature are given in Table 2. It
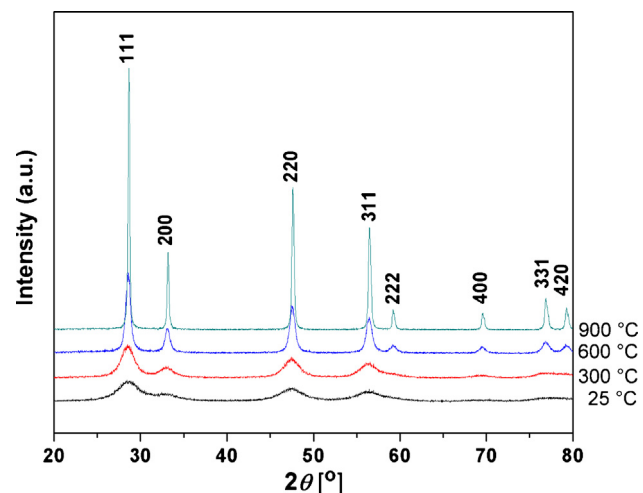
Table 2
Crystallite size (D), lattice parameters (a) and full width at half-maximum (FWHM) of $Ce_{0.80}Yb_{0.20}O_{2-\delta}$ powders calcined at different temperatures.

Temperature (°C)	FWHM	a (nm)	D (nm)
300	1.816	0.5420	11.2
600	0.615	0.5418	15.4
900	0.208	0.5412	61.8

was found that the crystallite size slightly increased from 11.2 nm for annealing temperature 300 °C to 15.4 nm for 600 °C. The average crystallite size of these samples was measured to be less than 20 nm. However, an increase in annealing temperature to 900 °C caused a considerable increase in crystallite size (>60 nm), indicating a better atomic arrangement in crystal lattice. This was in a good agreement with lattice parameter, which decreased with annealing
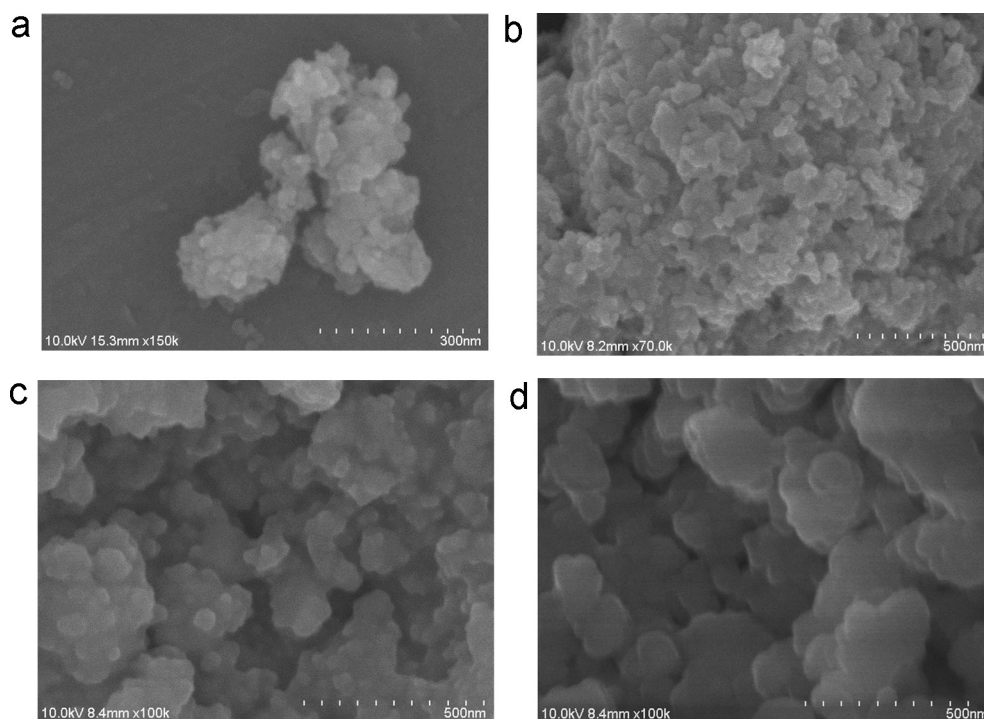

Fig. 4. FE-SEM micrographs of $Ce_{0.80}Yb_{0.20}O_{2-\delta}$ powders: (a) non-calcined and calcined at (b) 300 °C, (c) 600 °C and (d) 900 °C.
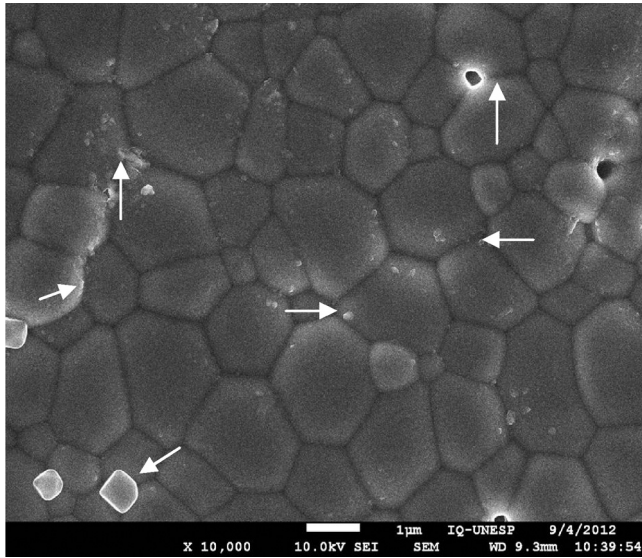
Fig. 5. SEM image of $Ce_{0.80}Yb_{0.20}O_{2-\delta}$ sintered at 1500 °C for 1 h in air atmosphere.

Fig. 6. Complex impedance plots of the sintered $Ce_{0.80}Yb_{0.20}O_{2-\delta}$ sample measured at 725 °C in air atmosphere.

temperature and approached to the value of the standard crystal lattice of ceria.

In Fig. 4(b)–(d), micrographs of $Ce_{0.80}Yb_{0.20}O_{2-\delta}$ powders calcined at different temperatures are shown. As a comparison, non-calcined powder is shown in Fig. 4(a). The microstructural observation of the annealed powder with $Ce_{0.80}Yb_{0.20}O_{2-\delta}$ composition showed agglomeration (Fig. 4) of individual crystals. Their sizes confirmed the XRD calculation; higher temperature leads to larger grains, however the size of crystals was still in nanometer range.

Micrograph of $Ce_{0.80}Yb_{0.20}O_{2-\delta}$ sintered at 1500 °C for 1 h is shown in Fig. 5. Microstructure was characterized as bimodal size distribution with the some amount of pores. The fraction of small grain around larger grains indicated that the mechanism of Ostwald ripening had been responsible for most of the grain growth observed. The grain size was in the range of 1–4 μm. Although the sample was very well sintered, a small number of curved grain boundaries could be noticed, which indicated that the sintering in some points was not finished, indicated in Fig. 5 with arrows.

Nyquist's diagrams (EIS graphs) of the sintered sample having the composition $Ce_{0.80}Yb_{0.20}O_{2-\delta}$ were recorded within the temperature range of 550–800 °C, with the increments of 25 °C. Impedance diagrams for various temperatures were selected to illustrate the impedance behavior of the doped ceria sample as a whole. As an example, the impedance graphs measured at 725 °C of $Ce_{0.80}Yb_{0.20}O_{2-\delta}$ is shown in Fig. 6. Generally, in the available frequency range, 0.1 Hz to 5 MHz, two adjacent remarkably distorted impedance semicircles were observed. Such a type of Nyquist plot is characteristic of two serially connected RC circuits, both of which containing one resistive and one capacitive element bonded in a parallel arrangement and the capacitive element being distributed (frequency dependent) one. Such an equivalent circuit with both constants [28–30] and distributed [31] capacitive elements has been widely applied for sintered ceramics. The high-frequency semicircle may be attributed to a parallel connection of the bulk resistance (R_{bulk}) of crystallite grains, and the geometric capacitance (C_{bulk}) of the sample. Those of low-frequency semicircle may be attributed to a parallel connection of the resistance (R_{gb}) of grain boundary phases, and the geometric capacitance (C_{gb}) of the grain boundary. If the impedance semicircles are clearly separated, i.e., $R_{bulk}C_{bulk} \ll R_{gb}C_{gb}$, the values of R_{bulk} and R_{gb} may be read separately as a intercept of the semicircles with the real axis.

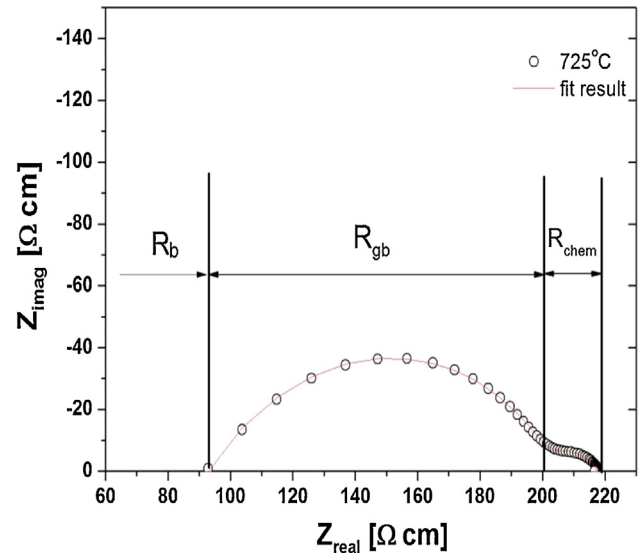As we can see in Fig. 6, there are three parts of graph: R_{bulk}, R_{gb} and R_{chem}. R_{bulk} is related to bulk resistance of the grains, R_{gb} is related to the resistance of grain boundary and R_{chem} is related to the processes that occur at the electrode/electrolyte interface. Marks in Fig. 6 for R_{bulk}, R_{gb} and R_{chem} are just an illustration and the real values of their parameters were obtained by fitting with the equivalent circuit that consists of two constant phase elements (CPE). With the decreasing of temperature, the values of R_{bulk}, R_{gb} and R_{chem} were increasing. As an example, in Fig. 7 are shown Nyquist diagrams (EIS graphs) for $Ce_{0.80}Yb_{0.20}O_{2-\delta}$ sample measured at the different temperatures. As could be seen in electrochemical impedance spectroscopy (Figs. 6 and 7), it is possible to determine the R_{bulk} and R_{gb} in the temperature interval of 550–800 °C. In addition, the possibility of separation of R_{bulk} and R_{gb} confirmed the success of the synthesis of ceria nanopowder by SPRT method. All values of resistivities (R_{bulk}, R_{gb}, R_{chem}) and conductivity (σ_{bulk}, σ_{gb}, σ_{chem}) for the sample $Ce_{0.80}Yb_{0.20}O_{2-\delta}$ are summarized in Table 3.

As it can be seen from Table 3, grain boundary resistivity dominated over the other resistivities. At 650 °C conductivity of bulk was 1.23×10^{-2} S/cm and that of grain boundary was 0.23×10^{-2} S/cm,
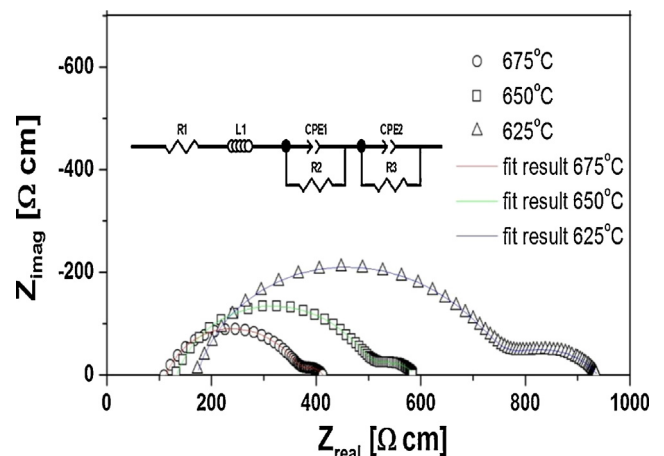

Fig. 7. Complex impedance plots of the sintered $Ce_{0.80}Yb_{0.20}O_{2-\delta}$ sample measured at different temperatures in air atmosphere.

Table 3
Values of R_{ohm}, R_{gb}, R_{chem}, σ_{ohm}, σ_{gb} and σ_{chem} for the sample $Ce_{0.80}Yb_{0.20}O_{2-\delta}$ at the different temperatures.

Temperature (°C)	Resistances (Ω cm)			Conductivities (10^{-2} S/cm)		
	R_{ohm}	R_{gb}	R_{chem}	σ_{ohm}	σ_{gb}	σ_{chem}
550	403.15	2002.14	2752.19	0.25	0.05	0.04
575	259.47	1304.84	1073.27	0.38	0.07	0.09
600	178.65	907.54	439.62	0.56	0.11	0.23
625	121.27	630.34	186.53	0.82	0.16	0.53
650	80.71	424.73	83.51	1.23	0.23	1.19
675	52.89	317.55	43.09	1.89	0.34	2.32
700	43.61	229.39	24.41	2.29	0.43	4.09
725	29.33	173.93	14.98	3.40	0.57	6.67
750	26.92	122.25	11.75	3.71	0.82	8.51
775	23.71	74.88	9.19	4.21	1.33	10.88
800	18.25	56.23	7.24	5.47	1.77	13.81
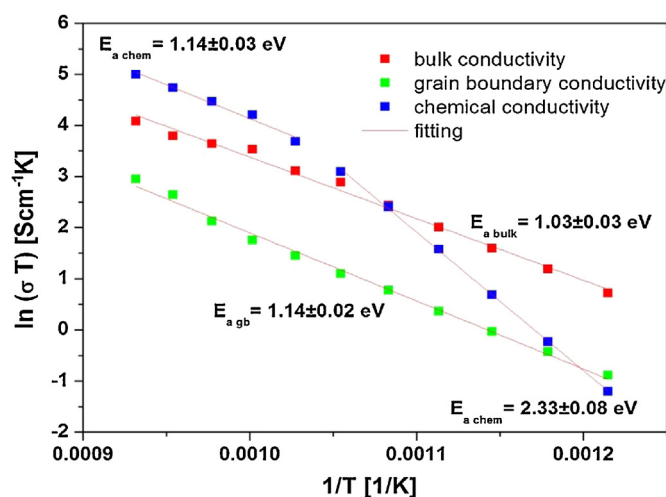
Fig. 8. Conductivities of the $Ce_{0.80}Yb_{0.20}O_{2-\delta}$ sample in the form of Arrhenius plots.

which was around one fifth of the bulk conductivity. In addition, comparing values of conductivity of present work with conductivity of similar materials based on oxygen ion conductors [32], it can be said that these values are very similar. In order to increase the conductivity of the $Ce_{0.80}Yb_{0.20}O_{2-\delta}$ sample, it is necessary to conduct investigation with aim to understand the conduction mechanism at the grain boundary of this material and to decrease the grain boundary resistance.

In Fig. 8, Arrhenius plots are shown of all three types of resistivity: R_{bulk}, R_{gb} and R_{chem}. Activation energies (E_a) were calculated from Arrhenius plots according to the derived equation:

$$\ln(\sigma \cdot T) = \ln A - \frac{E_a}{k} \cdot \frac{1}{T}$$ (4)

where σ is the conductivity, T is the absolute temperature, A is the pre-exponential factor and k is the Boltzmann constant. Activation energy for the bulk conduction was 1.03 eV and for grain boundary conduction was 1.14 eV. Based on researches reported by different authors and literature data [32,33], it can be concluded that the value of E_a in the present work is very similar activation energy for CeO_2 doped with dopants such as Sm^{3+}, Gd^{3+} and Nd^{3+} obtained by different methods. Also, similar values of activation energy were obtained for co-doped CeO_2 (Mg^{2+} and Sr^{2+}, Sm^{3+} and Gd^{3+}) [34,35]. However, comparing the obtained values of E_a with activation energies of similar materials based on oxygen ion conductors containing 15% and 20% dopants [26], our E_a values were significantly lower. It can be said that this is a consequence of well-ordered structure in the synthesis of nanopowder SPRT method, which allows easier activation of conductivity carriers and decrease E_a.

The existence of semicircles at lower frequencies (Fig. 7) in Nyquist diagrams is caused by electrochemical reactions that occur at the electrode/electrolyte interface. Almost doubtless, it originates from the oxygen electrode reactions, O_2/O^{2-}. In the case of these materials, we can say about the formation of oxygen ions described with the formula:

$$\frac{1}{2}O_2 + 2e^- \rightarrow O^{2-}$$ (5)

As we can see, the activation energy for this process had value 2.33 eV in the range of temperatures 550–675 °C and 675–800 °C the activation energy changed in the value 1.14 eV.

4. Conclusions

Nanostructured $Ce_{1-x}Yb_xO_{2-\delta}$ ($0 \le x \le 0.2$) oxides have been successfully synthesized by self-propagating room temperature method. Obtained powders have the fluorite crystal structure with space group *Fm3m*. It was found that the particle size lays in the nanometric range, less than 3 nm from XRD analysis. Particle size of powders increased during the heat treatment. After calcination at 600 °C, crystallite size reached the value up to 16 nm and after calcination at 900 °C crystallite size was larger than 60 nm. SEM analysis of calcined powders confirmed calculations of crystallite sizes obtained by XRD. However, after sintering at 1500 °C samples showed a bimodal size distribution with grain size in the range of 1–4 μm. Electrochemical impedance spectroscopy depicted that it was possible to separate R_{bulk} and R_{gb} in the temperature interval of 550–800 °C. The activation energy for the bulk conduction was 1.03 eV and for grain boundary conduction was 1.14 eV. Grain boundary resistivity dominates over the other resistivities. At 650 °C conductivity of bulk was 1.23×10^{-2} S/cm, which is around five times higher than conductivity of the grain boundary. This material has potential to be applied as an electrolyte for intermediate temperature SOFC, and additional investigations should be performed with aim to increase the conductivity of the grain boundary.

References

[1] X. Ma, X. Feng, X. He, H. Guo, L. Lv, J. Guo, H. Cao and T. Zhou, Microporous Mesoporous Mater., 158, 214–218 (2012).
[2] A.M.T. Silva, R.R.N. Marques and R.M. Quinta-Ferreira, Appl. Catal. B: Environ., 47, 269–279 (2004).
[3] S. Scirè, S. Minicò, C. Crisafulli, C. Satriano and A. Pistone, Appl. Catal. B: Environ., 40, 43–49 (2003).
[4] S.D. Randery, J.S. Warren and K.M. Dooley, Appl. Catal. A: Gen., 226, 265–280 (2002).
[5] Y.T. Kim and D.S. Shin, Appl. Phys. Lett, 71, 3507–3509 (1997).
[6] I. Lee, W.J. Lee and J. Yi, J. Korean Phys. Soc., 39, 57–61 (2001).
[7] M. Aguirre, M. Paulis and J.R. Leiza, J. Mater. Chem. A, 1, 3155–3162 (2013).
[8] D.H. Lee, K.S. Cha, Y.S. Lee, K.S. Kang, C.S. Park and Y.H. Kim, Int. J. Hydrogen Energy, 34, 1417–1422 (2009).
[9] N.Q. Minh, J. Am. Ceram. Soc., 76, 563–588 (1993).
[10] R.D. Shannon, Acta Crystallogr., A32, 751–767 (1976).
[11] N. Izu, W. Shin, I. Matsubara and N. Murayama, Sens. Actuator B: Chem., 94, 222–227 (2003).
[12] H. Inaba and H. Tagawa, Solid State Ionics, 83, 1–16 (1996).
[13] J.R. McBride, K.C. Hass, B.D. Poindexter and W.H. Weber, J. Appl. Phys., 76, 2435–2441 (1994).
[14] S. Tsunekawa, T. Fukuda and A. Kasuya, Surf. Sci. Lett., 457, L437–L440 (2000).
[15] B.C.H. Steele, Solid State Ionics, 129, 95–110 (2000).
[16] D. Terribile, A. Trovarelli, J. Llorca, C. de Leitenburg and G. Dolcetti, J. Catal., 178, 299–308 (1998).
[17] X. Yu, F. Li, X. Ye, X. Xin and Z. Xue, J. Am. Ceram. Soc., 83, 964–966 (2000).
[18] T. Tsuzuki and P.G. McCormik, J. Am. Ceram. Soc., 84, 1453–1458 (2001).
[19] T. Mokkelbost, I. Kaus, T. Grande and M. Einarsrud, Chem. Mater., 16, 5489–5494 (2004).
[20] S.B. Bošković, B.Z. Matović, M.D. Vlajić and V.D. Krstić, Ceram. Int., 33, 89–93 (2007).
[21] S. Gnanam and V. Rajendran, J. Sol–Gel Sci. Technol., 58, 62–69 (2011).
[22] S. Bošković, D. Đurović, Z. Dohčević-Mitrović, Z. Popović, M. Zinkevich and F. Aldinger, J. Power Sources, 145, 237–242 (2005).
[23] M. Stojmenović, S. Bošković, S. Zec, B. Babić, B. Matović, D. Bučevac, Z. Dohčević-Mitrović and F. Aldinger, J. Alloys Compd., 507, 279–285 (2010).
[24] M. Stojmenović, S. Bosković, D. Bucevac, M. Prekajski, B. Babić, B. Matović and S. Mentus, Ceram. Int., 39, 1249–1255 (2013).
[25] in Elements of X-Ray DiffractionB.D. Cullity and S.R. Stock, 3rd ed., Prentice Hall, New Jersey (2001).
[26] E.Yu. Pikalova, A.A. Murashkina, V.I. Maragou, A.K. Demin, V.N. Strekalovsky and P.E. Tsiakaras, Int. J. Hydrogen Energy, 36, 6175–6183 (2011).
[27] H. Yahiro, Y. Eguchi, K. Eguchi and H. Arai, J. Appl. Electrochem., 18, 527–531 (1988).
[28] R. Waster and R. Hagenbeck, Acta Mater., 48, 797–825 (2000).
[29] X.J. Chen, K.A. Khor, S.H. Chan and L.G. Yu, Mater. Sci. Eng., A341, 43–48 (2003).
[30] D. Pérez-Coll, P. Núñez and J.R. Frade, J. Power Sources, 196, 8383–8390 (2011).
[31] M.R. Kosinski and R.T. Baker, J. Power Sources, 196, 2498–2512 (2011).
[32] G. Kim, N. Lee, K.-B. Kim, B.-K. Kim, H. Chang, S.-J. Song and J.-Y. Park, Int. J. Hydrogen Energy, 38, 1571–1587 (2013).
[33] C. Veranitisagul, A. Kaewvilai, W. Wattanathana, N. Koonsaeng, E. Traversa and A. Laobuthee, Ceram. Int., 38, 2403–2409 (2012).
[34] N. Jaiswal, D. Kumar, S. Upadhyay and O. Parkash, J. Alloys Compd., 577, 456–462 (2013).
[35] W. Liu, B. Li, H. Liu and W. Pan, Electrochim. Acta, 56, 3334–3337 (2011).